Growth of NiTiO3 polymorphs on silicon substrates by radio frequency sputtering

Meriem Chettab, Quentin Simon, Mustapha Zaghrioui, Oleg I Lebedev, Xavier Rocquefelte, Gwenhael Duplaix-Rata, Richard Retoux, Patrick Laffez

To cite this version:

Meriem Chettab, Quentin Simon, Mustapha Zaghrioui, Oleg I Lebedev, Xavier Rocquefelte, et al.. Growth of NiTiO3 polymorphs on silicon substrates by radio frequency sputtering. Applied Surface Science, 2024, 669, pp.160381. 10.1016/j.apsusc.2024.160381 . hal-04600416

HAL Id: hal-04600416
https://hal.science/hal-04600416v1

Submitted on 4 Jul 2024

Growth of $NiTiO_3$ polymorphs on silicon substrates by radio frequency sputtering

Meriem CHETTAB[a], Quentin SIMON[a]*, Mustapha ZAGHRIOUI[a], Oleg I. LEBEDEV[b], Xavier ROCQUEFELTE[c], Gwenhael DUPLAIX-RATA[c], Richard RETOUX [b], Patrick LAFFEZ[a].*

a) *University of Tours, GREMAN, UMR 7347 – CNRS, IUT de Blois 15 Rue de la Chocolaterie 41029 BLOIS CEDEX*

b) *University of Caen, CRISMAT, UMR 6508 – CNRS, ENSICAEN 6 Bd Maréchal Juin, 14000 Caen,*

c) *University of Rennes, ISCR UMR6226 – CNRS, 263 Av. Général Leclerc, 35700 Rennes*

**Corresponding authors: Meriem CHETTAB, meriem.chettab@univ-tours.fr, Quentin SIMON, quentin.simon@univ-rennes.fr*

Abstract

Nickel titanate ($NiTiO_3$) is known to exhibit three types of structures which differ in terms of cationic ordering, namely ilmenite (IL), $LiNbO_3$ (LN), or corundum (CR) structures. In this study, radio frequency sputtering using Ar/O_2 reactive plasma has been used for the *in-situ* crystallization of $NiTiO_3$ thin films on Si(100) substrates heated at various temperatures (in the range 400°C-650°C). The stabilization of the different $NiTiO_3$ polymorphs as a function of the substrate's temperature are discussed basing on X-ray diffraction, Raman spectroscopy and high-resolution transmission electron microscopy characterizations. Depositions at 650°C enabled to obtain IL thin films. Depositions at lower temperature (400-600°C) led to the formation of mixture of IL/LN/CR structures. Whatever the substrate temperature, films are grown with a [00W] fiber texture. Post Annealing of the IL/LN/CR $NiTiO_3$ thin films at 800°C resulted in its recrystallization into the IL structure, while preserving the [00W] fiber texture.

Density functional theory (DFT) simulations aided in predicting Raman spectra for LN and CR phase. The combination of XRD, Raman spectroscopy, and HRTEM offers a detailed understanding of phase transitions and morphological changes, essential for optimizing the properties of $NiTiO_3$ films for various applications.

Key words:

thin film, nickel titanate, $NiTiO_3$, plasma sputtering, fiber texture, ilmenite, lithium niobate

1. Introduction

Multiferroics are materials which combine at least two ferroïc orders (magnetic, electric, elastic…). Development of new multiferroic materials has been of great interest in the last decade [1,2] for both fundamental [3,4] and technological [5,6] purposes. These developments have incited extensive research efforts aimed at exploiting the potential of multiferroic materials for a wide range of applications.

Expanding on the exploration of multiferroic materials, in a concise review, Ederer and Fennie [7] present their latest findings on electric field switching of magnetization in antiferromagnetic materials. Their work highlights that the Dzyaloshinskii-Moriya interaction [8,9] is driven by a ferroelectric distortion, resulting in a canting of antiferromagnetic moments, which gives rise to a weak ferromagnetic contribution. To achieve this canting effect, two conditions are necessary, as elucidated by Ederer and Fennie: *(i)* In the paraelectric phase, the inversion center coincides with the midpoint between two neighboring magnetic moments, which is disrupted by the ferroelectric transition, and *(ii)* the absence of symmetry operations prohibiting the system from displaying a macroscopic magnetization. [4] These conditions are satisfied in materials with the $LiNbO_3$ (LN) type structure. $FeTiO_3$, isomorphous to the LN structure, serves as an illustrative example. Indeed, materials of the general formula $ATiO_3$ with this structure, where A = Mn, Fe, and Ni, exhibit a favorable coupling between their polarization and magnetization. Among them, $NiTiO_3$ has been predicted to possess the largest magnetic moment ($M = 0.25\ \mu B/f.u.$). [4] Exploring multiferroic materials displaying this unique order, Varga *et al.* have investigated the $FeTiO_3$ system using high-temperature/high-pressure (HT/HP) synthesis, [10] and $NiTiO_3$ thin films through pulsed laser deposition (PLD) techniques. [11–13] In their work, Varga *et. al.* used different substrates such as Al_2O_3, $FeTiO_3$, and $LiNbO_3$ to induce epitaxial strain. This strain is necessary to stabilize a structure that satisfies the criteria outlined by Ederer and Fennie. [4]

Nickel Titanate ($NiTiO_3$ or NTO), possessing the centrosymmetric ilmenite (IL) structure, is an n-type antiferromagnetic semiconductor widely employed as a photocatalyst for the degradation of organic pollutants in water and for gas sensing. [14,15] The IL structure exhibits rhombohedral $R\overline{3}$ symmetry which is usually described in the hexagonal system as a stacking of layers formed by face-sharing oxygen octahedra, with Ni^{2+} and Ti^{4+} cations occupying two-thirds of the interstitial sites and alternating along the c-axis. [16,17] Titanates that spontaneously adopt the IL structure undergo crystallization under high pressure into a rhombohedral structure, isomorphous to $LiNbO_3$ (LN) compound with R3c symmetry. [18–21] LN structure can be described in a hexagonal lattice where the oxygen atoms accupy atomic positions similar to those of IL structure, while the cations arrange themselves along the three axes of the hexagonal lattice in the sequence Ni-Ti-□-Ni-Ti (where □ represents a vacant octahedral site). At high temperatures, the cations are disordered, and the titanate assumes a corundum (CR) structure with $R\overline{3}c$ symmetry which has so far been unquenchable and thus is challenging to stabilize at room temperature. [22,23]

The deposition of $NiTiO_3$ thin films displaying the IL structure has been reported by several groups using various methods, including chemical solution deposition, sputtering. [24,25] In contrary, few studies have addressed the obtention of LN and CR metastable phases. To this aim, note that the structuration of materials in thin films represents a valuable approach to access to high stress states on various systems, arising from epitaxial growth, [26] chemical stress, [27] or by residual stress. [28] Regarding the $NiTiO_3$ system, Varga *et al.* utilized pulsed laser deposition for the epitaxial growth of thin films exhibiting an LN identified structure, based on transmission electron microscopy observations and measurements of ferroic properties. [29] Bratvold *et al.* utilized atomic layer deposition to obtain epitaxially grown $NiTiO_3$ thin films, with reported structure being either LN or CR, given that these two structures cannot be discriminated by X-ray diffraction, as mentioned by the authors. [22]

The present study focuses on the deposition of $NiTiO_3$ thin films on Si(100) substrates by radio frequency (rf) magnetron co-sputtering starting from two metallic targets (Ni and Ti). RF magnetron sputtering is a technique that enables uniform thin film deposition on a large industrial scale [30] and Si substrates give the possibility of an easy integration into electronic devices. [31] In our previous work, a two-step process was developed to obtain single phase IL thin films with random orientation: i) room temperature deposition of NiTi thin films in pure Ar plasma, ii) post-annealing at 800°C in air. [32] In the present work, the process has been modified to obtain in a single-step the in-situ crystallization of $NiTiO_3$ polymorphs. Reactive sputtering was used to promote the in-situ oxidation of Ni and Ti species using Ar/O_2 plasma. In addition, thermal energy was supplied during the deposition process by heating the silicon substrate. In a first part of this paper, the effect of substrate temperature on the stabilizing of the three possible structures of $NiTiO_3$ is presented: ilmenite (IL, $R\overline{3}$), $LiNbO_3$-type (LN, R3c), and corundum (CR, $R\overline{3}c$). In order to discriminate these phases, global and local structural characterization techniques were used by combining X-ray diffraction, Raman Spectroscopy supported by theoretical calculation along with high-resolution transmission electron microscopy analyses. In a second part of the paper, the effect of ex-situ annealing is presented.

2. Material and methods

Radio frequency magnetron sputtering:

Radio frequency (RF) magnetron sputtering was employed for the co-deposition of $NiTiO_3$ thin films on Si (100) substrates. Prior to deposition, the Si (100) substrates underwent a thorough cleaning process involving successive rinsing in soapy water, deionized water, acetone, and isopropanol. The deposition chamber was evacuated to a base pressure of 10^{-4} Pa using a combination of a primary pump and a turbo molecular pump. The thin films were deposited from two inches metallic targets of nickel and titanium, each one connected to its own radio-frequency power generator. The targets were tilted in a converging configuration towards the substrate, and the substrate-to-target distance was set to 9 cm. The depositions were carried out in a reactive atmosphere of Ar/O_2, with an Ar flux of 25 sccm and an O_2 flux of 1 sccm. The working pressure was regulated to 1.5 Pa by adjusting the aperture between the deposition chamber and the pumping system.

For achieving a thin film composition with an atomic ratio of Ti:Ni = 1, the radio-frequency power was maintained at 20 W on the Ni cathode, while the power on the Ti target was adjusted in the range of 50–100 W. The cationic composition was then adjusted using a process adapted from previous work, which is detailed in the supplementary information. [32,33] To obtain thin films with atomic ratios Ti:Ni = 1 for a deposition pressure of 1.5 Pa, RF powers were set as follows: 96 W on Ti target and 20 W on Ni target. Before each deposition, the targets were sputtered for 30 minutes to ensure homogeneous surface state. The deposition time was varied between 120 and 180 min leading to film thickness ranging from 60 to 120 nm. During the deposition, the substrate holder was heated and connected to a rotation system to ensure uniform deposition.

Annealing:

After the deposition process, annealing of the $NiTiO_3$ samples is conducted on selected samples in a tubular furnace at 600°C or 800°C during 1h under 10 sccm of O_2 flow. The heating and cooling rates were set at 4°C/min.

Scanning electron microscopy (SEM) and energy dispersive X-ray spectroscopy (EDX):

Surface morphology was examined by scanning electron microscopy (SEM), using a TESCAN microscope equipped with a Field Emission Gun operating at 10 kV. To analyze chemical composition, energy dispersive X-ray spectroscopy (EDX) is employed with an acceleration voltage of 15 kV and a working distance of 15 mm. Six positions were probed for each sample to ensure homogeneity, and the compositions were calculated through a deconvolution of the recorded EDX spectra using Oxford Instrument AZTec software.

X Rays Diffraction (XRD):

X-ray diffraction (XRD) patterns were obtained using a Bruker D8 advance diffractometer with Cu radiations (kα1 = 1.54056 Å and kα2 = 1.54439 Å). Bragg-Brentano θ-2θ scans were performed for phase identification, and the patterns were fitted using highScore software. [34] Prior to each fit, sample height was corrected using Si 400 diffraction peak of the substrate as an internal reference. The c lattice parameter of the unit cell was extracted, from the fit results, using the 2θ Bragg position of the 006 reflection.

X rays reflectometry (XRR):

Thickness measurements were determined through X-ray reflectometry (XRR) using a parallel X-ray beam and analyzed with Bruker's Leptos software.

Raman spectroscopy:

Raman scattering measurements were conducted using a Renishaw Invia Reflex spectrometer in the backscattering geometry, employing a non-polarized 633 nm wavelength with a power of 2 mW. An x50 lens was used to focus and to collect the incident beam and the scattered light, respectively.

Transmission electron microscopy:

Transmission Electron Microscopy (TEM) and Electron spectroscopy investigations were carried out using a cold FEG JEM ARM200F microscope, operated at 200 kV, and equipped with a CENTURIO EDX detector, ORIUS Gatan camera, and Quantum GIF. The TEM analysis included bright-field high-resolution TEM (BF HRTEM), high-angle annular dark-field scanning transmission electron microscopy (HAADF-STEM), selected area electron diffraction (SAED), and simultaneous energy-dispersive X-ray (EDX) elemental mapping experiments. HAADF-STEM image simulations were performed using JEMS software. Cross sections TEM samples were prepared by Focused Ion Beam (FIB) technique using standard protocol.

Theoretical Calculations

Theoretical calculations were performed within Density Functional Theory (DFT) using the Vienna ab initio Simulation Package (VASP). [35–37] The Generalized Gradient approximation (GGA) with Perdew, Burke, and Ernzehof (PBE) functional was employed for electron exchange and correlation. [38] Atom cores are described through the projector augmented wave (PAW) method. [39] The kinetic energy cutoff for plane wave expansions was set to 550 eV, and the Brillouin zone was sampled by Monkhorst–Pack meshes of 8x8x8. [40] Atomic positions were optimized until forces were converged to lower than 1.10^{-2} eV/Å. Since the localized 3d states of Ni are not properly treated in DFT, a Hubbard U correction has been added using GGA+U method [41] with U = 4.5 eV and the Hund's coupling constant J = 0.9 eV. These parameters allow to properly describe the spin state of Ni in these systems.

The Raman spectra have been simulated using both Phonopy and Phono3py packages, [42,43] based on Density Functional Perturbation Theory (DFPT) calculations using VASP. Four models have been intended. The first two correspond to IL and LN phases with $R\overline{3}$ and R3c space groups, respectively, both treated using the primitive unit cell (a_p x b_p x c_p) corresponding to the rhombohedral setting. The remaining two models were designed to account for the partial occupancy of the cationic site by Ni and Ti, and were described in a $2a_P$ x b_P x c_P supercell.

3. Results and discussions

In a first series of experiment, the deposition temperature was varied within the range of 400°C to 650°C to determine the *in-situ* crystallization temperature of $NiTiO_3$ samples.

Figure 1 shows the SEM cross section of two representative samples deposited at 550°C (Figure 1(a)) and 650°C (Figure 1(b)). Both cross sections show the columnar growth characteristic of sputtering deposition. Nonetheless, while the sample deposited at 650°C presents well defined columns with sharped tips, the sample deposited at 550°C appears to be composed of more closely packed columns with flatter surface. The flatter surface of the sample deposited at 550°C is also shown in plane view SEM images (Figure S2 in SI) exhibiting less rugosity for the lower deposition temperature. This observation needs to be supported by other characterization techniques with lower limit of detection as HRTEM in the following part of this work. Regardless of deposition temperature, the thicknesses of the films were close to 120 nm (deposition time: 180 min), as also systematically confirmed by XRR on the whole series of samples.

Figure 2(a) shows the θ-2θ XRD scans of the samples deposited at different temperatures. For some XRD patterns (*e.g.* 500°C and 550°C), a diffraction peak at 2θ =33.15° is present. This peak is related to the forbidden diffraction from silicon substrate. [44]

To identify the IL, LN, and CR structures, it is noteworthy to mention their respective diffraction conditions. The IL structure has a single diffraction condition: -h + k + l = 3n. In contrast, both the LN and CR structures have four identical diffraction conditions and cannot be distinguished by XRD technique. The first diffraction condition is the same as that for the IL structure: -h + k + l = 3n. The remaining three, systematic diffraction conditions, are as follows: *0 k l : l = 2n, h 0 l : l = 2n, 0 0 l : l = 2n*. [45] Therefore, if a sample is *00l* oriented, we expect *00l* diffraction peaks with *l = 3n* in the case of IL structure (*e.g.* 003, 006, 009, 0012…) and *l = 2n* in the case of LN and CR structures (*e.g.* 006, 0012 …).

In the XRD patterns of Figure 2(a), a weak diffraction peak at 2θ = 39.02° is observed for the sample deposited at 400°C indicating the starting of crystallization. This peak becomes more intense above 500°C and can be attributed to the (006) planes of the $NiTiO_3$ polymorphs described in the hexagonal symmetry. At 650°C, the XRD pattern shows two diffraction peaks at 2θ = 19.33° et 2θ = 39.24°. These peaks are assigned to the (003) and (006) atomic planes of IL phase. [46] The relative intensity $\frac{I_{003}}{I_{006}} = 0.33$ which is comparable to the one reported for $NiTiO_3$ IL bulk material ($\frac{I_{003}}{I_{006}} = 0.30$). [46]

Therefore, and according to the diffraction conditions cited above, for deposition temperature ranging from 400°C to 600°C the sample structure is either LN or CR (noted LN/CR) or a mix of both, while for 650°C, the sample structure appears to be mainly IL. As the diffraction patterns display solely *00l* reflections, the samples consequently demonstrate a [00W] fiber texture. This means that the *c* axis of the lattice is perpendicular to the substrate with a rotational degree of freedom around this axis since no in-plane ordering has been observed (not shown here).

The out-of-plane *c* lattice parameter, extracted from 006 peak position in θ-2θ scans, is plotted as function of substrate temperature in Figure 2(b). The two green dashed lines indicate the *c* parameters of bulk $NiTiO_3$ IL (13.79 Å) [46] and LN-type structures (13.85 Å) reported in literature. [47] The *c* parameter gradually decreases as the substrate temperature increases from 500°C to 600°C, and presents a significant reduction when the substrate temperature reaches 650°C. In the range 500-600°C, the *c* lattice parameter is close to that of LN-type structure reported by Varga *et al.*. [47] At 650°C, this parameter becomes smaller than the bulk value of IL $NiTiO_3$ structure and is also comparable to that of IL $NiTiO_3$ thin films ($c = 13.77$ Å) reported by Bellam *et al.*. These results support that a substrate temperature of 650°C is necessary to obtain IL phase. Below this temperature, alternative structures are obtained (LN and/or CR). Nonetheless, a lattice parameter reduction upon the formation of IL phase may be surprising. Indeed, the transition from IL to LN structures was reported to be accompanied by a decrease of the unit cell volume in bulk $FeTiO_3$. [48] The described reduction in unit cell volume has not been observed in either $NiTiO_3$ thin films or in the $NiTiO_3$ bulk phase. The unit cell volume for the LN $NiTiO_3$ has been simulated by Varga *et al.* [47] and is expected to be smaller than the IL unit cell volume. In their experiments, Varga group successfully obtained $NiTiO_3$ thin films in the LN structure with a lattice parameter $c = 13.85$ Å. This c parameter is larger than the IL bulk value similarly to our results. This can be explained by stress resulting from the structuration in the films. In fact, a compressive strain reduce the in-plane parameters (a and b) and elongates the c parameter. [49] Therefore, the significant reduction of the out-of-plane lattice parameters in our results when the substrate temperature is raised form 600°C to 650°C may be the consequence of stress relaxation upon the crystallization of IL structure.

It is noteworthy that the temperature required for the *in situ* crystallization of IL $NiTiO_3$ in this work (650°C) is lower than those required for the *ex situ* crystallization (*i.e.* sputtering deposition at low temperature followed by annealing in air) as reported in our previous work (800°C) or by Bellam *et al.* (1100°C).[32,50] Also, *in situ* growth induces a [00W] fiber texture while random orientation is obtained during *ex situ* growth.

To provide further support for the crystallization of $NiTiO_3$ thin films in diverse structures, additional symmetry characterizations were conducted using Raman spectroscopy. This non-destructive technique provides vibrational modes corresponding to symmetry elements in a crystal structure. Raman spectroscopy can differentiate between IL, LN and CR symmetries by identifying their distinct vibrational modes. On one hand the Raman signature of $NiTiO_3$ IL is well-documented, [51–54] on the other hand, no experimental or theoretical Raman spectrum has been reported for $NiTiO_3$ LN and CR phases to the best of our knowledge. Thus, DFT Raman simulations have been performed to predict Raman spectra for every phase. The DFT optimized cell parameters for IL and LN $NiTiO_3$ are, respectively, a = 5.07 Å and c = 13.91 Å, and a = 5.05 Å and c = 13.97 Å, in excellent agreement with the experimental ones (less than 1% deviation). It is interesting to notice that our calculations reproduce the 0.06 Å increase of the c parameter from IL to LN structures.

A comparison between experimental data and our DFT Raman simulation, after rescaling the frequencies, is proposed in Figure 3 for IL phase. Calculated PBU+U frequencies deviate from the experimental ones by about 24 cm^{-1} in average. It should be noticed that such an underestimation is expected using PBE functional. After applying a scaling factor of s = 1.066, the mean deviation is reduced to 1 cm^{-1}. The resulting spectrum is in good agreement with the experimental data in terms of intensity and frequency. As shown in Figure 3 (green curve), the Raman spectrum consists of 10 vibrational modes ($5A_g+5E_g$) with the main mode around 705 cm^{-1}. [51]

The PBE+U approach combined to a scaling factor of 1.066 has also been used to predict the vibrational frequencies of LN phase (blue spectrum in Figure 3). Its spectrum should contain 13 vibrational modes ($4A_1$+9E) according to symmetry considerations. [55] The Raman signature of LN phase appears to be significantly different from that of IL phase, spanning from 215 cm^{-1} to 630 cm^{-1}, and the most intense peak is simulated for a Raman shift of 432 cm^{-1}, where no intense Raman signal is expected for IL phase. This feature could thus be a good candidate to discriminate LN and IL phases. In contrast, the second most intense peak (E mode) has a Raman shift of 247 cm^{-1}, very close to the A_g mode of IL phase which is measured at 249 cm^{-1}. It is thus inadequate to differentiate the two phases.

Regarding the CR structure, for which the cations are disordered, the simulations of the Raman spectrum is quite challenging. In order to efficiently consider the Ni/Ti disorder of the CR phase within a reasonable calculation timeframe, we have created two models using a $2a_P$ x b_P x c_P supercell. The resulting optimized cell parameters are closer to the IL structure than LN ones with a = 5.05 and c = 13.91 Å. Figure 4 presents the schematic representation of the primitive cell for IL (Figure 4 (a), (b)) and LN (Figure 4 (c)) phases, and two models of CR phase (Figure 4(d), (e)) used to simulate Raman spectra. Simulated spectra of the former cells show that high frequency modes are very sensitive to the introduction of chemical disorder. These modes observed at 723 cm^{-1} and 785 cm^{-1}, respectively for IL and LN phases are located at 749 cm^{-1} and 773 cm^{-1} for the model represented in Figure 4(d), and at 747 cm^{-1} and 754 cm^{-1} for the model represented in Figure 4(e). Note that the mode of LN at 785 cm^{-1} corresponds to A_2 symmetry which is an inactive Raman mode.

The introduction of Ni/Ti disorder in the cation occupation renders this mode A_2 Raman active due to the modification of the second neighbors of the cations. This alteration significantly affects the local symmetry and, consequently, the vibrational degrees of freedom. These modes are potential candidates for the assignment of the experimental vibration mode located at 780 cm^{-1}.

Figure 5 displays the experimental Raman spectra of $NiTiO_3$ samples deposited at various temperatures, ranging from 400°C to 650°C. At 400°C and 500°C, the Raman spectrum is primarily composed of silicon substrate vibration modes, along with a peak at 780 cm^{-1}, which can be attributed to the CR phase, as predicted by previous simulations. As the deposition temperature is raised to 550°C and 600°C, the intensity of the CR vibration mode increases, and a new vibration mode emerges at 705 cm^{-1}. This newly observed mode is associated with the main vibration mode of the IL phase. [50] In addition, two modes are detected at 435 cm^{-1} and 620 cm^{-1}. Both are a contribution of Si and LN phase vibrations as demonstrated by DFT simulations (Figure 3). Upon further increasing of the deposition temperature to 650°C, an additional mode of the IL structure becomes evident at 393 cm^{-1}, while the intensity of the CR and LN modes decreases. This observation suggests a further enhancement of the crystallization into the IL phase. [50]

The results obtained by XRD and Raman spectroscopy can be summarized as follows. At 400°C, a weak diffraction peak is observed on XRD scan while the Raman spectrum indicates the initial stage of CR phase formation. Between 500°C and 600°C, XRD and Raman results support the formation of LN/CR phases. Nonetheless, in this temperature range, Raman spectroscopy also reveals the appearance of IL phase from 550°C. At 650°C, both techniques indicate the formation of IL structure as the majority phase with small residue of LN/CR structure still detected by Raman spectroscopy. In conclusion, a gradual transition from LN/CR to IL structure as the deposition temperature increases is observed. The differences between the two techniques are due to the fact that Raman spectroscopy is more sensitive to local ordering while XRD is sensitive to longer range ordering. In order to attain more local information of phase formation, HR-TEM characterizations have been carried out.

Two representative samples were selected for TEM characterization. A sample deposited at 650°C (S1) and a sample deposited at 550°C (S2). Both samples were deposited at 1.5 Pa for 2 h. The estimation of their thickness by XRR revealed slight difference, with 80 and 60 nm for S1 and S2, respectively.

Figure 6 presents the TEM results obtained for sample S1 deposited at 650°C. The low-magnification bright-field TEM image (Figure 6(a)) and the high-angle annular dark-field scanning transmission electron microscopy (HAADF-STEM) overview image (Figure 6(b)) indicate that the $NiTiO_3$ thin film presents a columnar growth with appreciable roughness and a thickness of about 80 nm, in agreement with SEM and XRR characterizations. The grain width varies within the range of 20-50 nm.

Figure 6(c) shows a high-resolution HAADF-STEM image along [110] zone axis of a well-defined single column. In this image, the representation of the *c* axis of the IL structure (same as fiber axis) perpendicular to the substrate surface confirms the texture growth supported by XRD data. In addition, the surface of this grain is faceted by {014} and {015} planes, as evidenced by the white lines (Figure 6(c)). Note that the {104} planes have the lowest surface energy in IL structure and are therefore, the most stable. [58–60]

Figure 6(d) and (e) shows high resolution HAADF-STEM images of S1 along two most informative [100] and [210] zone axis. According to image simulation performed on IL ($NiTiO_3$ ilmenite, rhombohedral $R\overline{3}$ SG $a=5.04Å$, $c=13.81Å$ ICSD1544718) structure, and LN ($NiTiO_3$, rhombohedral $R3c$) structures (Fig S1, supplementary information), only the HAADF-STEM images along [100] and [210] zone axis allows to distinguish the two closely related structures due to difference in particular contrast of atomic columns. The HAADF-STEM images (Figure 6 (c), (d)) reveal a good crystalline quality, free of defects and stacking faults. Performed image simulations (Figure 6(c), (d) insert) based on IL structure shows perfect fitting with the experimental image confirming the obtained XRD and Raman spectroscopy results for sample deposited at substrate temperature of 650°C.

Figure 7 and Figure 8 depict TEM results for S2 sample deposited at 550°C. In the low magnification cross-section HAADF-STEM image, along with simultaneously acquired EDX-STEM elemental mapping ((Figure 7(a)), we observe a uniform contrast, flat $NiTiO_3$ film with a typical thickness of approximately 60 nm. All elements are homogeneously distributed over the film. In the high resolution HAADF-STEM in (Figure 7(b)), it can be seen that the film consists of grain widths ranging from 15 nm to 30 nm separated by low angle grain boundaries. In contrast to the S1 film, Figure 7 reveals that no faceting is observed in the S2 film. The surface appears flat and sharp, in line with the SEM observations (Figure 1). Additionally, the high resolution HAADF-STEM image of S2 (Figure 7(b)) depicts a region consisting of three $NiTiO_3$ [210]-oriented grains separated by thin intermediate layers appearing at the grain boundaries (GBs). The width of these intermediate layers is approximately 5 nm and exhibit epitaxial local intergrowth between the grains.

To determine the structure of the film, both in the grains or in intermediate layers at the grain boundaries, a meticulous analysis of HAADF-STEM images was conducted. Owing in mind homogeneous distribution of all elements (Figure 7(a)) with accordance to the nominal composition, this analysis involved image simulations based on potential structures, including IL, LN, and CR. The contrast within $NiTiO_3$ grains is not uniform, unlike the case of the S1 film, (Figure 7(b)). According to the simulation of the [210] HAADF-STEM image (Fig S1), the Ni/Ti atomic columns display equivalent intensity bright contrast, and this type of contrast predominates throughout the image (Figure 8). The performed image simulation of LN structure along [210] zone axis shows good agreement with experiment (Figure 8(b)). Therefore, most of these grains belong to the LN structure. Nevertheless, the typical contrast of the IL structure along the [210] projection, where atomic column brightness alternates (one out of two, as shown in S1), is also locally observed. This observation leads to the conclusion that the film in the S2 sample contains a mixture of LN and IL phases, as previously deduced from X-ray diffraction (XRD) and Raman characterizations. In the same time, the contrast of the GBs intermediate layers in HAADF-STEM images cannot be fitted with LN or IL structures but could corresponds to CR domains. Keeping in mind the growth conditions and considering the available literature reports, we conducted a thorough analysis of specific contrasts in the image and their corresponding Fourier transform (FT) patterns. When taking all the data into consideration, it becomes apparent that the corundum-type $NiTiO_3$ structure may provide an explanation for these contrasts, as previously reported in the literature. [22] The structure file was generated using corundum structure (rhombohedral Al_2O_3) where Ni and Ti randomly occupy the same position. The simulated HAADF-STEM image and ED pattern of this corundum $NiTiO_3$ structure along [301] zone axis shows good agreement with obtained experimental image (Figure 8(c)).

In conclusion, HRTEM corroborates XRD and Raman spectroscopy characterization. Sample S1 is confirmed to be an ilmenite (IL) $NiTiO_3$ thin film, while S2 is a mixture of IL and LN grains with CR grain boundaries (GBs). It appears that the CR grain boundaries represent a mechanism for strain relaxation from LN domains to IL domains within the film. When the sample is mostly IL, the columnar structure is exhibited. When the sample is a mix of LN, CR and IL, an intergrowth between phases is observed and leads to a flat surface of the sample.

Finally, the influence of post-deposition annealing on the structural features of $NiTiO_3$ thin films was investigated. To this end, a set of 3 $NiTiO_3$ thin films were simultaneously deposited in the same conditions as S2: deposition duration of 2 h at a substrate temperature of 550°C. After the deposition, one sample was kept as-deposited while the two others were annealed under O_2 flux for 1 h at 600°C and 800°C. Figure 9(a), (b) and (c) show SEM images of the as-deposited and post-annealed samples at 600°C and 800°C, respectively. Figure 9(a) and (b) are alike and present thin films with a granular surface. This indicates that no morphology change occurs during an annealing at 600°C. In a different way, Figure 9(c) shows that an annealing temperature of 800°C promotes a grain coarsening.

Figure 9(d) shows XRD patterns of the as-deposited and post-annealed samples. The as-deposited sample produces an XRD pattern owning a unique diffraction peak due to (006) atomic plane of $NiTiO_3$ phase as obtained in the previous section. The sample has LN/CR structure with a [00W] fiber texture. No significant change in XRD pattern is recorded after annealing at 600°C. Therefore, this temperature preserves the LN/CR structure and crystal orientation of the sample. After annealing at 800°C a 003 diffraction peak is detected, revealing that the crystalline structure of the sample changed to IL. The *c* lattice parameters and relative intensities $\frac{I_{003}}{I_{006}}$ for the as-deposited and annealed samples are extracted from XRD patterns showed in Figure 9(d). The *c* lattice parameter of the as-deposited sample at 550°C is 13.85 Å. This parameter decreases with increasing annealing temperature to 13.81 Å at 600°C and 13.76 Å at 800°C, in agreement with the formation of relaxed IL structure. In addition, the relative intensity $\frac{I_{003}}{I_{006}} = 0.27$ is comparable to the one found for $NiTiO_3$ IL bulk material ($\frac{I_{003}}{I_{006}} = 0.30$). [46]

Figure 10 shows Raman spectra of samples deposited at 550°C and post-annealed. The as-deposited samples at 550°C exhibit CR, LN and Si substrate vibration modes. The CR and LN vibration modes relative intensity decreases after annealing at 600°C and disappear after annealing at 800°C. After this annealing, only IL vibration modes are detected. Raman spectra corroborates XRD results. At a deposition temperature of 550°C, a mix of IL and LN/CR phases are formed. Annealing at 600°C results in a reduction of the LN/CR phase contribution, with a shift in favor of the IL phase. At 800°C, pure IL phase is observed in the limit of detection of the technique.

4. Conclusion

In conclusion, this study sheds light on the crucial role of thermal energy in the in-situ crystallization process of $NiTiO_3$ thin films deposited by multitarget reactive RF magnetron sputtering. Through meticulous examination of deposition temperatures, the research discerns a clear correlation between temperature variations and resultant crystalline phases. Lower temperatures foster the formation of layered (LN) and corundum (CR) structures due to surface defect trapping of ad-atoms, while higher temperatures facilitate the diffusion of ad-atoms, promoting the crystallization of the more stable ilmenite (IL) phase.

The comprehensive multi-scale structural characterization, encompassing X-ray diffraction (XRD), Raman spectroscopy, and transmission electron microscopy (TEM), allows for the differentiation of LN, CR, and IL structures. While XRD analysis relies on diffraction conditions and lattice parameters, Raman spectroscopy, complemented by density functional theory (DFT) calculations, proves instrumental in discriminating LN and CR structures. Furthermore, simulations of high-angle annular dark-field scanning transmission electron microscopy (HAADF-STEM) images enable the distinction between IL and LN structures based on contrast variations.

The findings elucidate a systematic transition from LN/CR phases to IL structure as the deposition temperature increases. This transition is observed to be gradual, with LN/CR phases coexisting within grains, while CR phases predominantly reside at grain boundaries, facilitating strain relaxation. Notably, this study marks the first observation of LN/CR structures and achieves in-situ IL texture growth on silicon substrates, holding significant implications for electronic device integration.

In essence, this research contributes to a deeper understanding of the intricate interplay between thermal energy, deposition conditions, and resultant crystalline phases in $NiTiO_3$ thin films. Such insights are pivotal for the tailored synthesis of materials with desired properties, thereby paving the way for advancements in electronic device technologies

5. Bibliography

[1] N.A. Hill, Why Are There so Few Magnetic Ferroelectrics?, J. Phys. Chem. B 104 (2000) 6694–6709. https://doi.org/10.1021/jp000114x.

[2] M. Fiebig, T. Lottermoser, D. Meier, M. Trassin, The evolution of multiferroics, Nat. Rev. Mater. 1 (2016) 16046. https://doi.org/10.1038/natrevmats.2016.46.

[3] T. Zhao, A. Scholl, F. Zavaliche, K. Lee, M. Barry, A. Doran, M.P. Cruz, Y.H. Chu, C. Ederer, N.A. Spaldin, R.R. Das, D.M. Kim, S.H. Baek, C.B. Eom, R. Ramesh, Electrical control of antiferromagnetic domains in multiferroic BiFeO3 films at room temperature, 5 (2006) 7.

[4] C.J. Fennie, Ferroelectrically Induced Weak Ferromagnetism by Design, Phys. Rev. Lett. (2008) 4.

[5] S. Hajra, V. Vivekananthan, M. Sahu, G. Khandelwal, N.P.M. Joseph Raj, S.-J. Kim, Triboelectric nanogenerator using multiferroic materials: An approach for energy harvesting and self-powered magnetic field detection, Nano Energy 85 (2021) 105964. https://doi.org/10.1016/j.nanoen.2021.105964.

[6] N. Hur, S. Park, P.A. Sharma, J.S. Ahn, S. Guha, S.-W. Cheong, Electric polarization reversal and memory in a multiferroic material induced by magnetic fields, Nature 429 (2004) 392–395. https://doi.org/10.1038/nature02572.

[7] C. Ederer, C.J. Fennie, Electric-field switchable magnetization via the Dzyaloshinskii--Moriya interaction: FeTiO3 versus BiFeO3, J Phys (2008) 9.

[8] T. Moriya, Anisotropic Superexchange Interaction and Weak Ferromagnetism, Phys. Rev. 120 (1960) 91–98. https://doi.org/10.1103/PhysRev.120.91.

[9] I. Dzyaloshinsky, A thermodynamic theory of “weak” ferromagnetism of antiferromagnetics, J. Phys. Chem. Solids 4 (1958) 241–255. https://doi.org/10.1016/0022-3697(58)90076-3.

[10] T. Varga, A. Kumar, E. Vlahos, S. Denev, M. Park, S. Hong, T. Sanehira, Y. Wang, C.J. Fennie, S.K. Streiffer, X. Ke, P. Schiffer, V. Gopalan, J.F. Mitchell, Coexistence of Weak Ferromagnetism and Ferroelectricity in the High Pressure LiNbO3-Type Phase of FeTiO3, Phys. Rev. Lett. (2009) 4.

[11] T. Varga, Controlling the structure and ferroic properties of strained epitaxial NiTiO3 thin films on sapphire by post-deposition annealing, Thin Solid Films (2018) 7.

[12] T. Varga, T.C. Droubay, M.E. Bowden, R.J. Colby, S. Manandhar, D. Hu, B.C. Kabius, E. Apra, W.A. Shelton, S.A. Chambers, Coexistence of weak ferromagnetism and polar lattice distortion in epitaxial NiTiO3 thin films of the LiNbO3-type structure, J Vac Sci Technol B 31 (2013) 6.

[13] T. Varga, T.C. Droubay, M.E. Bowden, L. Kovarik, D. Hu, S.A. Chambers, Strain-Dependence of the Structure and Ferroic Properties of Epitaxial NiTiO3 Thin Films Grown on Different Substrates, Adv. Condens. Matter Phys. (n.d.) 10.

[14] J.B. Bellam, M.A. Ruiz-Preciado, M. Edely, J. Szade, A. Jouanneaux, A.H. Kassiba, Visible-light photocatalytic activity of nitrogen-doped NiTiO $_3$$ thin films prepared by a co-sputtering process, RSC Adv. 5 (2015) 10551–10559. https://doi.org/10.1039/C4RA12516A.

[15] J. Huang, Y. Jiang, G. Li, C. Xue, W. Guo, Hetero-structural NiTiO 3 /TiO 2 nanotubes for efficient photocatalytic hydrogen generation, Renew. Energy 111 (2017) 410–415. https://doi.org/10.1016/j.renene.2017.04.024.

[16] T.F.W. Barth, E. Posnjak, The Crystal Structure of Ilmenite., Z. Für Krist. - Cryst. Mater. 88 (1934) 265–270. https://doi.org/10.1524/zkri.1934.88.1.265.

[17] R.P. Liferovich, R.H. Mitchell, Rhombohedral ilmenite group nickel titanates with Zn, Mg, and Mn: synthesis and crystal structures, (n.d.) 8.

[18] R.S. Weis, T.K. Gaylord, Lithium niobate: Summary of physical properties and crystal structure, Appl. Phys. Solids Surf. 37 (1985) 191–203. https://doi.org/10.1007/BF00614817.

[19] H.D. Megaw, A note on the structure of lithium niobate, LiNbO3, Acta Crystallogr. A 24 (1968) 583–588. https://doi.org/10.1107/S0567739468001282.

[20] J.Y. Son, G. Lee, M.-H. Jo, H. Kim, H.M. Jang, Y.-H. Shin, Heteroepitaxial Ferroelectric ZnSnO $_3$ Thin Film, J. Am. Chem. Soc. 131 (2009) 8386–8387. https://doi.org/10.1021/ja903133n.

[21] A.M. Arévalo-López, J.P. Attfield, Weak ferromagnetism and domain effects in multiferroic LiNbO 3 -type MnTiO 3 -II, Phys. Rev. B 88 (2013) 104416. https://doi.org/10.1103/PhysRevB.88.104416.

[22] J.E. Bratvold, H. Fjellvåg, O. Nilsen, Phase and Orientation Control of NiTiO3 Thin Films, Materials 13 (2019) 112. https://doi.org/10.3390/ma13010112.

[23] J.E. Bratvold, H. Fjellvåg, O. Nilsen, Atomic Layer Deposition of oriented nickel titanate (NiTiO3), Appl. Surf. Sci. 311 (2014) 478–483. https://doi.org/10.1016/j.apsusc.2014.05.092.

[24] J.B. Bellam, M.A. Ruiz-Preciado, M. Edely, J. Szade, A. Jouanneaux, A.H. Kassiba, Visible-light photocatalytic activity of nitrogen-doped NiTiO $_3$$ thin films prepared by a co-sputtering process, RSC Adv. 5 (2015) 10551–10559. https://doi.org/10.1039/C4RA12516A.

[25] P. C., M. W., Electrical and magnetic properties of NiTiO3 nanoparticles synthesized by the sol–gel synthesis method and microwave sintering, J. Mater. Res. Technol. 8 (2019) 3097–3101. https://doi.org/10.1016/j.jmrt.2017.07.007.

[26] J.H. Lee, L. Fang, E. Vlahos, X. Ke, Y.W. Jung, L.F. Kourkoutis, J.-W. Kim, P.J. Ryan, T. Heeg, M. Roeckerath, V. Goian, M. Bernhagen, R. Uecker, P.C. Hammel, K.M. Rabe, S. Kamba, J. Schubert, J.W. Freeland, D.A. Muller, C.J. Fennie, P. Schiffer, V. Gopalan, E. Johnston-Halperin, D.G. Schlom, A strong ferroelectric ferromagnet created by means of spin–lattice coupling, Nature 466 (2010) 954–958. https://doi.org/10.1038/nature09331.

[27] O. Copie, J. Varignon, H. Rotella, G. Steciuk, P. Boullay, A. Pautrat, A. David, B. Mercey, P. Ghosez, W. Prellier, Chemical Strain Engineering of Magnetism in Oxide Thin Films, Adv. Mater. 29 (2017) 1604112. https://doi.org/10.1002/adma.201604112.

[28] E. Chason, B.W. Sheldon, L.B. Freund, J.A. Floro, S.J. Hearne, Origin of Compressive Residual Stress in Polycrystalline Thin Films, Phys. Rev. Lett. 88 (2002) 156103. https://doi.org/10.1103/PhysRevLett.88.156103.

[29] T. Varga, T.C. Droubay, M.E. Bowden, L. Kovarik, D. Hu, S.A. Chambers, Strain-Dependence of the Structure and Ferroic Properties of Epitaxial NiTiO3 Thin Films Grown on Different Substrates, Adv. Condens. Matter Phys. (n.d.) 10.

[30] V.J.C. Rigi, M.K. Jayaraj, K.J. Saji, Envisaging radio frequency magnetron sputtering as an efficient method for large scale deposition of homogeneous two dimensional MoS2, Appl. Surf. Sci. 529 (2020) 147158. https://doi.org/10.1016/j.apsusc.2020.147158.

[31] T. Ando, X.-A. Fu, Materials: Silicon and beyond, Sens. Actuators Phys. 296 (2019) 340–351. https://doi.org/10.1016/j.sna.2019.07.009.

[32] M. Chettab, Influence of sputtering conditions and annealing parameters on structure and morphology of NiTiO3 ilmenite thin films, Thin Solid Films (2020) 6.

[33] P. Laffez, Q. Simon, Y. Kikuchi, R. Retoux, F. Giovannelli, A. Yamamoto, Growth of polycrystalline Pr_4\$$Ni_3$\$$O_{10}$\$ thin films for intermediate temperature solid oxide fuel cell cathode by radio frequency magnetron co-sputtering, Thin Solid Films 693 (2020) 137705. https://doi.org/10.1016/j.tsf.2019.137705.

[34] T. Degen, M. Sadki, E. Bron, U. König, G. Nénert, The HighScore suite, Powder Diffr. 29 (2014) S13–S18. https://doi.org/10.1017/S0885715614000840.

[35] G. Kresse, J. Furthmüller, Efficiency of ab-initio total energy calculations for metals and semiconductors using a plane-wave basis set, Comput. Mater. Sci. 6 (1996) 15–50. https://doi.org/10.1016/0927-0256(96)00008-0.

[36] G. Kresse, J. Hafner, Ab initio molecular-dynamics simulation of the liquid-metal–amorphous-semiconductor transition in germanium, Phys Rev B 49 (1994) 14251–14269. https://doi.org/10.1103/PhysRevB.49.14251.

[37] G. Kresse, J. Furthmüller, Efficient iterative schemes for ab initio total-energy calculations using a plane-wave basis set, Phys Rev B 54 (1996) 11169–11186. https://doi.org/10.1103/PhysRevB.54.11169.

[38] J.P. Perdew, K. Burke, M. Ernzerhof, Generalized Gradient Approximation Made Simple [Phys. Rev. Lett. 77, 3865 (1996)], Phys Rev Lett 78 (1997) 1396–1396. https://doi.org/10.1103/PhysRevLett.78.1396.

[39] P.E. Blöchl, Projector augmented-wave method, Phys Rev B 50 (1994) 17953–17979. https://doi.org/10.1103/PhysRevB.50.17953.

[40] H.J. Monkhorst, J.D. Pack, Special points for Brillouin-zone integrations, Phys Rev B 13 (1976) 5188–5192. https://doi.org/10.1103/PhysRevB.13.5188.

[41] S.L. Dudarev, G.A. Botton, S.Y. Savrasov, C.J. Humphreys, A.P. Sutton, Electron-energy-loss spectra and the structural stability of nickel oxide: An LSDA+U study, Phys Rev B 57 (1998) 1505–1509. https://doi.org/10.1103/PhysRevB.57.1505.

[42] A. Togo, L. Chaput, T. Tadano, I. Tanaka, Implementation strategies in phonopy and phono3py, J. Phys. Condens. Matter 35 (2023) 353001. https://doi.org/10.1088/1361-648X/acd831.

[43] A. Togo, First-principles Phonon Calculations with Phonopy and Phono3py, J. Phys. Soc. Jpn. 92 (2023) 012001. https://doi.org/10.7566/JPSJ.92.012001.

[44] P. Zaumseil, High-resolution characterization of the forbidden Si 200 and Si 222 reflections, J. Appl. Crystallogr. 48 (2015) 528–532. https://doi.org/10.1107/S1600576715004732.

[45] T.R. Welberry, ed., International Tables for Crystallography: Mathematical, physical and chemical tables, 2nd ed., International Union of Crystallography, Chester, England, 2021. https://doi.org/10.1107/97809553602060000117.

[46] R.P. Liferovich, R.H. Mitchell, Rhombohedral ilmenite group nickel titanates with Zn, Mg, and Mn: synthesis and crystal structures, Phys. Chem. Miner. 32 (2005) 442–449. https://doi.org/10.1007/s00269-005-0020-7.

[47] T. Varga, T.C. Droubay, M.E. Bowden, P. Nachimuthu, V. Shutthanandan, T.B. Bolin, W.A. Shelton, S.A. Chambers, Epitaxial growth of NiTiO3 with a distorted ilmenite structure, Thin Solid Films 520 (2012) 5534–5541. https://doi.org/10.1016/j.tsf.2012.04.060.

[48] L.C. Ming, Y.-H. Kim, T. Uchida, Y. Wang, M. Rivers, In situ X-ray diffraction study of phase transitions of $FeTiO_3$ at high pressures and temperatures using a large-volume press and synchrotron radiation, Am. Mineral. 91 (2006) 120–126. https://doi.org/10.2138/am.2006.1930.

[49] G. Abadias, E. Chason, J. Keckes, M. Sebastiani, G.B. Thompson, E. Barthel, G.L. Doll, C.E. Murray, C.H. Stoessel, L. Martinu, Review Article: Stress in thin films and coatings: Current status, challenges, and prospects, J. Vac. Sci. Technol. Vac. Surf. Films 36 (2018) 020801. https://doi.org/10.1116/1.5011790.

[50] J.B. Bellam, M.A. Ruiz-Preciado, M. Edely, J. Szade, A. Jouanneaux, A.H. Kassiba, Visible-light photocatalytic activity of nitrogen-doped $NiTiO_3$ thin films prepared by a co-sputtering process, RSC Adv. 5 (2015) 10551–10559. https://doi.org/10.1039/C4RA12516A.

[51] M.I. Baraton, G. Busca, M.C. Prieto, G. Ricchiardi, V.S. Escribano, On the Vibrational Spectra and Structure of FeCrO3 and of the Ilmenite-Type Compounds CoTiO3 and NiTiO3, J. Solid State Chem. 112 (1994) 9–14. https://doi.org/10.1006/jssc.1994.1256.

[52] G. Busca, G. Ramis, P. Piaggio, FT Raman and FTlR Studies of Titanias and Metatitanate Powders, J CHEM SOC FARADAY TRANS 90 (1994) 10.

[53] R.V. Rodrigues, E.J.B. Muri, P.C.M. da Cruz, A.A.L. Marins, L.U. Khan, R.M. Oliveira, J.R. Matos, H.F. Brito, L.C. Machado, Thermogravimetric study on preparation of NiTiO3

in different reaction times, J. Therm. Anal. Calorim. 126 (2016) 1499–1505. https://doi.org/10.1007/s10973-016-5836-5.

[54] A.M. Hofmeister, IR reflectance spectra of natural ilmenite: comparison with isostructural compounds and calculation of thermodynamic properties, Eur. J. Mineral. 5 (1993) 281–296. https://doi.org/10.1127/ejm/5/2/0281.

[55] K. Fujita, T. Kawamoto, I. Yamada, O. Hernandez, N. Hayashi, H. Akamatsu, W. Lafargue-Dit-Hauret, X. Rocquefelte, M. Fukuzumi, P. Manuel, A.J. Studer, C.S. Knee, K. Tanaka, LiNbO $_3$ -Type InFeO $_3$: Room-Temperature Polar Magnet without Second-Order Jahn–Teller Active Ions, Chem. Mater. 28 (2016) 6644–6655. https://doi.org/10.1021/acs.chemmater.6b02783.

[56] M.A. Ruiz-Preciado, A. Bulou, M. Makowska-Janusik, A. Gibaud, A. Morales-Acevedo, A. Kassiba, Nickel titanate (NiTiO $_3$$) thin films: RF-sputtering synthesis and investigation of related features for photocatalysis, CrystEngComm 18 (2016) 3229–3236. https://doi.org/10.1039/C6CE00306K.

[57] P. Sinha, S.E. Boesch, C. Gu, R.A. Wheeler, A.K. Wilson, Harmonic Vibrational Frequencies: Scaling Factors for HF, B3LYP, and MP2 Methods in Combination with Correlation Consistent Basis Sets, J. Phys. Chem. A 108 (2004) 9213–9217. https://doi.org/10.1021/jp048233q.

[58] L. Li, C. Zhang, Z. Yuan, Z. Liu, C. Li, Selectivity of Benzyl Hydroxamic Acid in the Flotation of Ilmenite, Front. Chem. 7 (2019) 886. https://doi.org/10.3389/fchem.2019.00886.

[59] R.A.P. Ribeiro, J. Andrés, E. Longo, S.R. Lazaro, Magnetism and multiferroic properties at MnTiO$_3$$ surfaces: A DFT study, Appl. Surf. Sci. 452 (2018) 463–472. https://doi.org/10.1016/j.apsusc.2018.05.067.

[60] W. Sun, V. Ageh, H. Mohseni, T.W. Scharf, J. Du, Experimental and computational studies on stacking faults in zinc titanate, Appl. Phys. Lett. 104 (2014) 241903. https://doi.org/10.1063/1.4883747.

List of figures

Figure 1: SEM cross section of NiTiO3 thin films deposited for 3 h at 550°C (a) and 650°C (b). The scale is indicated by the white bar. The thickness for each sample is estimated at 120 nm

Figure 2: (a) XRD diffraction patterns of $NiTiO_3$ thin films, deposited at different temperatures (film thickness: 120 nm), (b) Out-of-plane lattice parameters c of the thin films of NiTiO3 as a function of substrate temperature.

Figure 3: DFT simulations of the Raman spectra of both IL ($R\bar{3}$) and LN (R3c) phases of $NiTiO_3$. The experimental Raman spectrum of the IL phase is given for comparison. [56] The irreducible characters are provided. A scaling factor of 1.06 has been applied to the PBE+U values reducing the exp./theo. deviation from 24 to 1 cm^{-1} for IL phase. It allows to propose a prediction of the Raman shifts for LN phase. The calculation of the scaling factor was done using $s = \sum_i \left(w_i^{calc} w_i^{exp}\right) / \sum_i \left(w_i^{calc}\right)^2$, with w_i^{calc} and w_i^{exp} the calculated and experimental frequencies, respectively, expressed in cm^{-1}. [57]

Figure 4: (a) Schematic representation of the primitive cell $NiTiO_3$ in the IL phase along a axis. Views along c axis of (b) the IL phase, (c) the LN phase, and (d & e) the two CR models (oxygen atoms are not shown for simplicity).

Figure 5: Raman spectra of thin films of $NiTiO_3$ deposited at different substrate temperatures (from 400°C to 650°C). A broken axis is used for the sake of clarity in order to suppress the very intense peak of Si substrate located at 520 cm^{-1}.

Figure 6: TEM images of S1: $NiTiO_3$ thin film deposited on Si(100) substrate at 650°C. (a) Cross-section bright field overview of the thin film, (b) low magnification cross-section HAADF-STEM image of $NiTiO_3$ film, (c) High resolution HAADF-STEM image of the surface of single $NiTiO_3$ grain viewing along [110] zone axis. Noticed faceting of the grain along {014} and {015} planes, (d) high resolution HAADF-STEM image of the single grain along [100] zone axis. Magnified image together with overlapping simulated image and structural model are given in the insert. (e) high resolution HAADF-STEM image of the single grain along [210] zone axis. Magnified image together with overlapping simulated image and structural model are given in the insert. Image simulation was done based on IL structure.

Figure 7: TEM images of S2: $NiTiO_3$ thin film deposited on Si(100) substrate at 550°C and 1.5 Pa. (a) Low magnification HAADF-STEM image and simultaneously acquired EDX-

STEM elemental maps for Ti K, Ni K, Si K. O K and overplayed color image. (b) high resolution [210] HAADF-STEM image of selected by black box in (a) area of $NiTiO_3$ film. The intergrowth secondary phase at $NiTiO_3$ grains boundaries marked by red arrows.

Figure 8: TEM images of S2: $NiTiO_3$ thin film deposited on Si(100) substrate at 550°C. (a) High resolution HAADF-STEM image of grain boundary region of $NiTiO_3$ film deposited at a pressure of 1.5 Pa and a substrate temperature of 550°C on Si substrate viewed along [210] zone axis. Red arrows depict the GBs (b) high resolution [210] HAADF-STEM image of $NiTiO_3$ grain and corresponding FT pattern. Simulated image based on LN structure is given in the insert in magnified image (left panel) (c) high resolution HAADF-MSTEM image of GB and corresponding FT pattern. The simulated image of GB structure based on $NiTiO_3$ CR is given in the insert. FT pattern is superposition of [210] $NiTiO_3$ LN (white rectangle) and [301] $NiTiO_3$ CR structure (red box).

Figure 9: SEM micrographs of thin films deposited simultaneously for 2 h at 1.5 Pa and 550°C :(a) as deposited and post-annealed under oxygen flow at (b) 600°C and (c) 800°C. (d)Diffraction patterns of these thin films

Figure 10: Raman spectra of thin films simultaneously deposited for 2 h at 1.5 Pa and 550°C and annealed under oxygen flow at 600°C and 800°C. A broken axis is used for the sake of clarity in order to suppress the very intense peak of Si substrate located at 520 cm^{-1}.

Figures

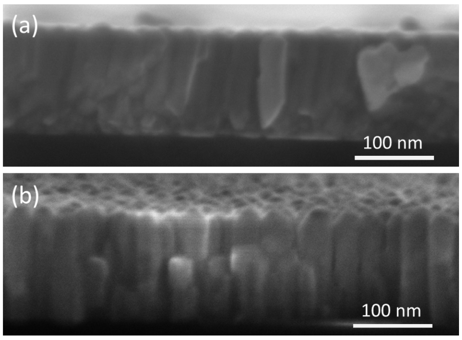

Figure 1: SEM cross section of $NiTiO_3$ *thin films deposited for 3 h at 550°C (a) and 650°C (b). The scale is indicated by the white bar. The thickness for each sample is estimated at 120 nm*

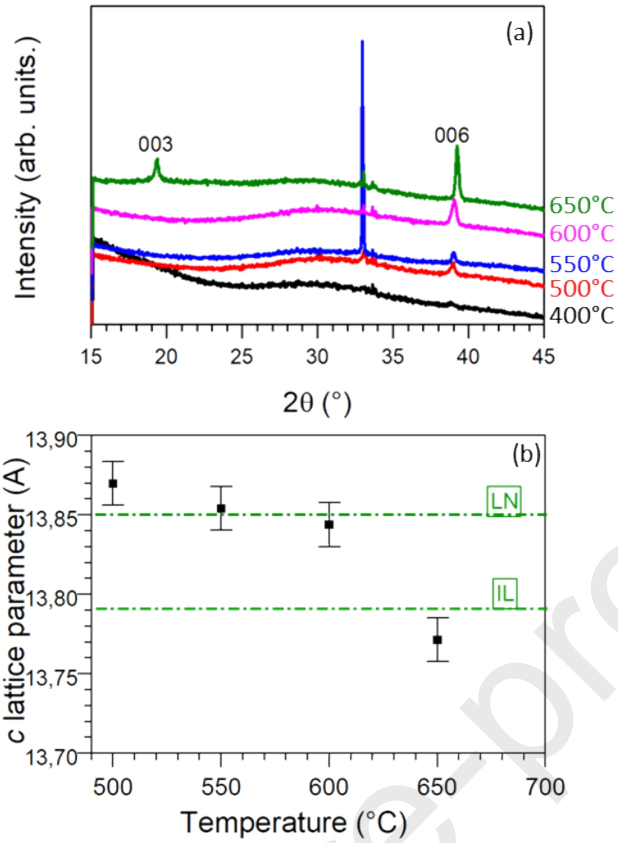

Figure 2: (a) XRD diffraction patterns of $NiTiO_3$ thin films, deposited at different temperatures (film thickness : 120 nm), (b) Out-of-plane lattice parameters c of the thin films of $NiTiO_3$ as a function of substrate temperature.

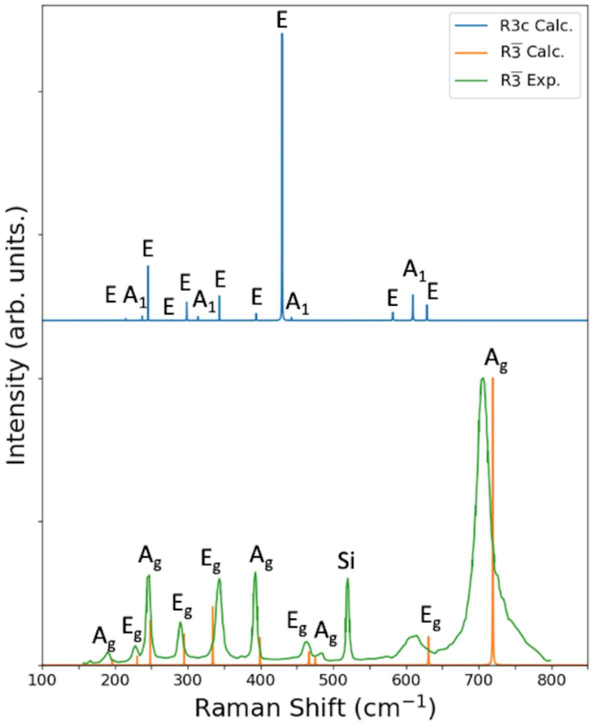

Figure 3: DFT simulations of the Raman spectra of both IL (R$\overline{3}$) and LN (R3c) phases of NiTiO$_3$. The experimental Raman spectrum of the IL phase is given for comparison. [56] The irreducible characters are provided. A scaling factor of 1.06 has been applied to the PBE+U values reducing the exp./theo. deviation from 24 to 1 cm^{-1} for IL phase. It allows to propose a prediction of the Raman shifts for LN phase. The calculation of the scaling factor was done using $s = \sum_i (w_i^{calc} w_i^{exp}) / \sum_i (w_i^{calc})^2$, with w_i^{calc} and w_i^{exp} the calculated and experimental frequencies, respectively, expressed in cm^{-1}. [57]

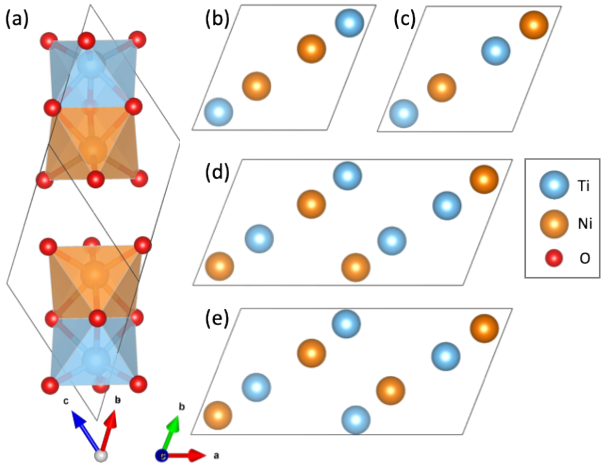

Figure 4: (a) Schematic representation of the primitive cell $NiTiO_3$ *in the IL phase along a axis. Views along c axis of (b) the IL phase, (c) the LN phase, and (d & e) the two CR models (oxygen atoms are not shown for simplicity).*

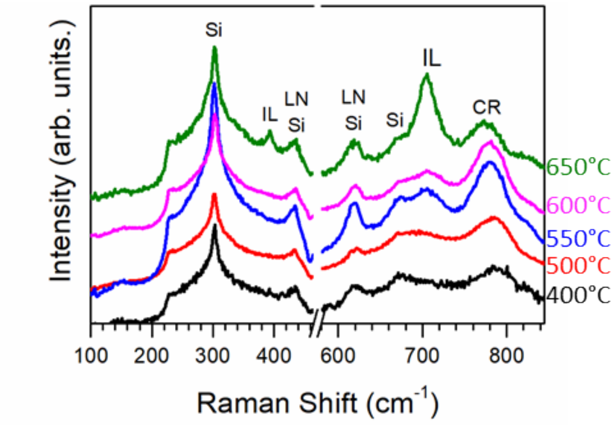

Figure 5: Raman spectra of thin films of $NiTiO_3$ *deposited at different substrate temperatures (from 400°C to 650°C). A broken axis is used for the sake of clarity in order to suppress the very intense peak of Si substrate located at 520 cm*$^{-1}$.

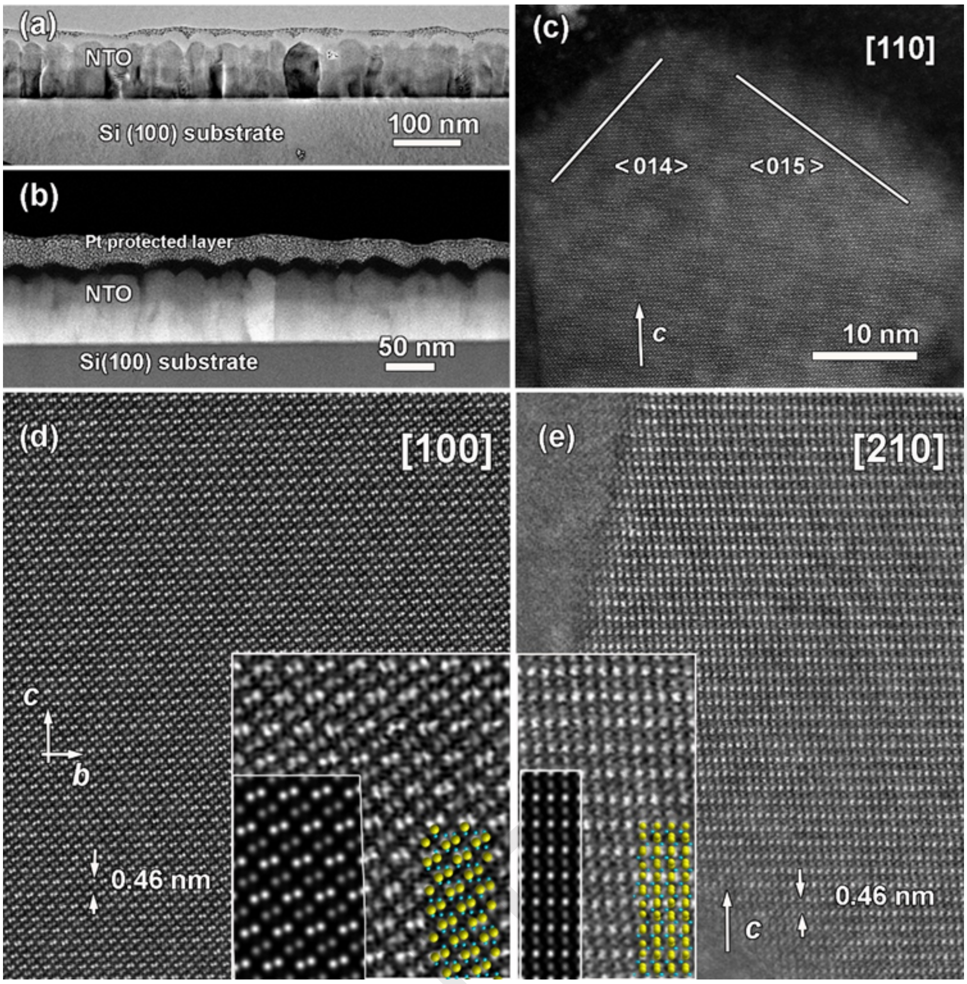

Figure 6: TEM images of S1: NiTiO$_3$ thin film deposited on Si(100) substrate at 650°C. (a) Cross-section bright field overview of the thin film, (b) low magnification cross-section HAADF-STEM image of NiTiO$_3$ film, (c) High resolution HAADF-STEM image of the surface of single NiTiO$_3$ grain viewing along [110] zone axis. Noticed faceting of the grain along {014} and {015} planes, (d) high resolution HAADF-STEM image of the single grain along [100] zone axis. Magnified image together with overlapping simulated image and structural model are given in the insert. (e) high resolution HAADF-STEM image of the single grain along [210] zone axis. Magnified image together with overlapping simulated image and structural model are given in the insert. Image simulation was done based on IL structure.

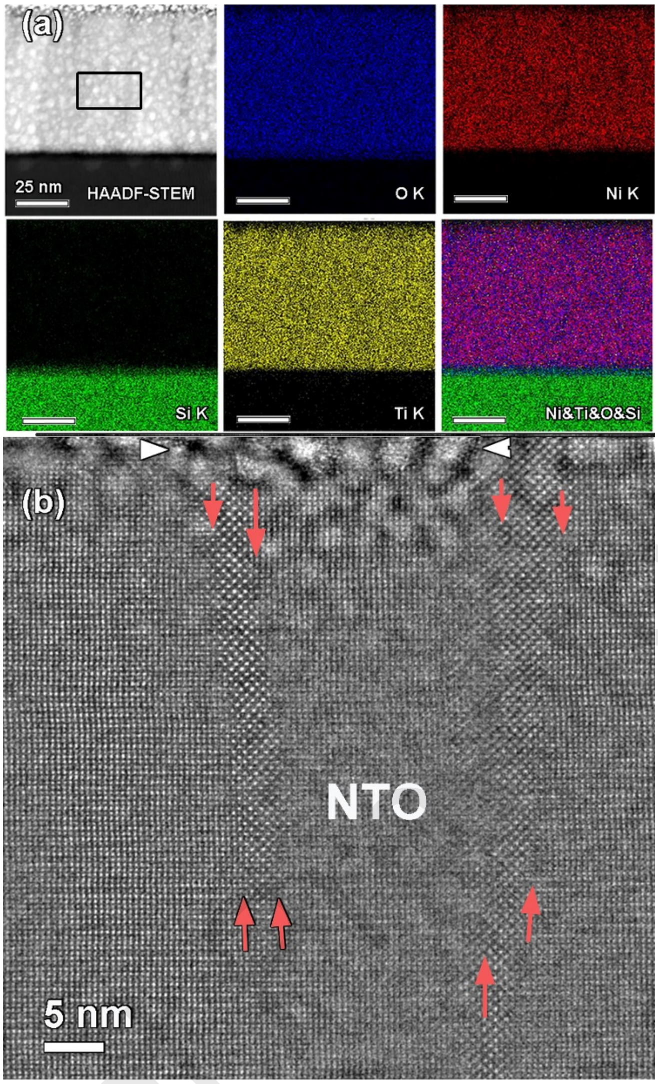

Figure 7: TEM images of S2: $NiTiO_3$ thin film deposited on Si(100) substrate at 550°C and 1.5 Pa. (a) Low magnification HAADF-STEM image and simultaneously acquired EDX-STEM elemental maps for Ti K, Ni K, Si K. O K and overplayed color image. (b) high resolution [210] HAADF-STEM image of selected by black box in (a) area of $NiTiO_3$ film. The intergrowth secondary phase at $NiTiO_3$ grains boundaries marked by red arrows.

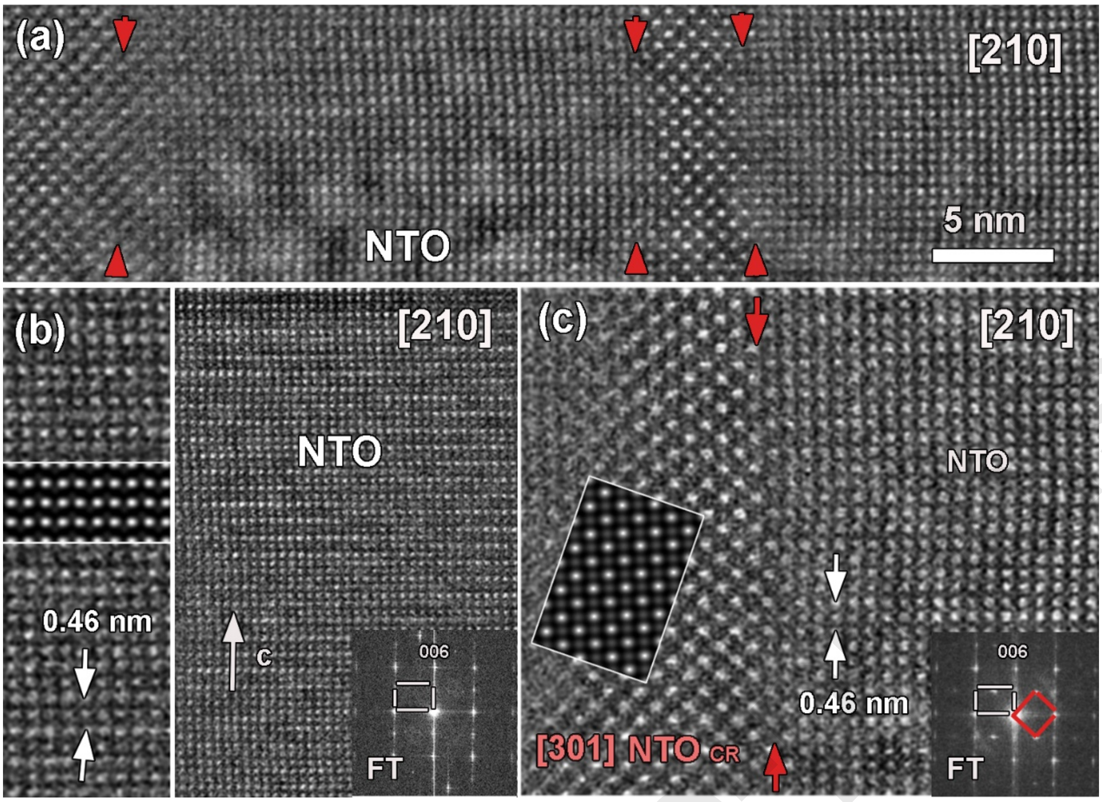

Figure 8: TEM images of S2: $NiTiO_3$ thin film deposited on Si(100) substrate at 550°C. (a) High resolution HAADF-STEM image of grain boundary region of $NiTiO_3$ film deposited at a pressure of 1.5 Pa and a substrate temperature of 550°C on Si substrate viewed along [210] zone axis. Red arrows depict the GBs (b) high resolution [210] HAADF-STEM image of $NiTiO_3$ grain and corresponding FT pattern. Simulated image based on LN structure is given in the insert in magnified image (left panel) (c) high resolution HAADF-MSTEM image of GB and corresponding FT pattern. The simulated image of GB structure based on $NiTiO_3$ CR is given in the insert. FT pattern is superposition of [210] $NiTiO_3$ LN (white rectangle) and [301] $NiTiO_3$ CR structure (red box).

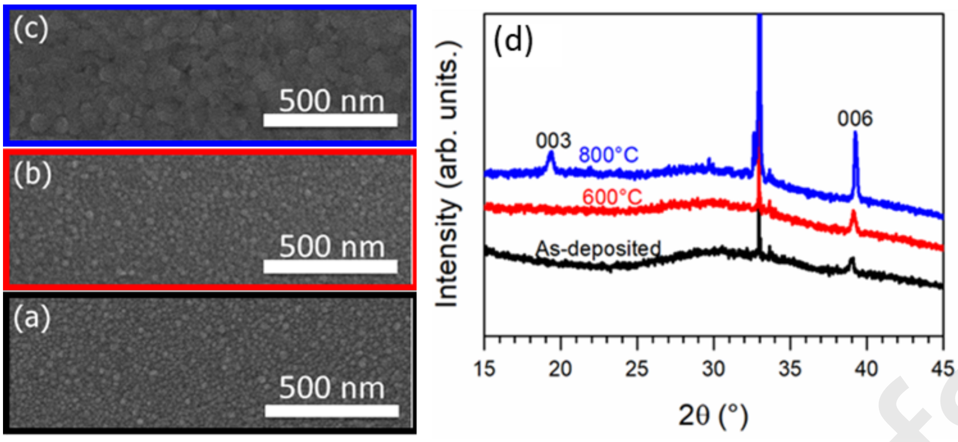

Figure 9: SEM micrographs of thin films deposited simultaneously for 2 h at 1.5 Pa and 550°C :(a) as deposited and post-annealed under oxygen flow at (b) 600°C and (c) 800°C. (d)Diffraction patterns of these thin films

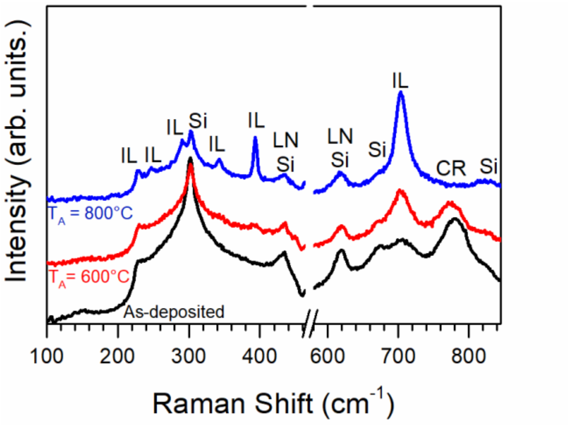

Figure 10: Raman spectra of thin films simultaneously deposited for 2 h at 1.5 Pa and 550°C and annealed under oxygen flow at 600°C and 800°C. A broken axis is used for the sake of clarity in order to suppress the very intense peak of Si substrate located at 520 cm^{-1}.

Acknowledgements: The theoretical work benefited from access to the HPC resources of TGCC/CINES/IDRIS under Allocation No. 2020-A0090907682 provided by GENCI.

List of figures

Figure 1: SEM cross section of NiTiO3 thin films deposited for 3 h at 550°C (a) and 650°C (b). The scale is indicated by the white bar. The thickness for each sample is estimated at 120 nm

Figure 2: (a) XRD diffraction patterns of $NiTiO_3$ thin films, deposited at different temperatures (film thickness: 120 nm), (b) Out-of-plane lattice parameters c of the thin films of NiTiO3 as a function of substrate temperature.

Figure 3: DFT simulations of the Raman spectra of both IL ($R\overline{3}$) and LN (R3c) phases of $NiTiO_3$. The experimental Raman spectrum of the IL phase is given for comparison. [56] The irreducible characters are provided. A scaling factor of 1.06 has been applied to the PBE+U values reducing the exp./theo. deviation from 24 to 1 cm^{-1} for IL phase. It allows to propose a prediction of the Raman shifts for LN phase. The calculation of the scaling factor was done using $s = \sum_i \left(w_i^{calc} w_i^{exp}\right) / \sum_i \left(w_i^{calc}\right)^2$, with w_i^{calc} and w_i^{exp} the calculated and experimental frequencies, respectively, expressed in cm^{-1}. [57]

Figure 4: (a) Schematic representation of the primitive cell $NiTiO_3$ in the IL phase along a axis. Views along c axis of (b) the IL phase, (c) the LN phase, and (d & e) the two CR models (oxygen atoms are not shown for simplicity).

Figure 5: Raman spectra of thin films of $NiTiO_3$ deposited at different substrate temperatures (from 400°C to 650°C). A broken axis is used for the sake of clarity in order to suppress the very intense peak of Si substrate located at 520 cm^{-1}.

Figure 6: TEM images of S1: $NiTiO_3$ thin film deposited on Si(100) substrate at 650°C. (a) Cross-section bright field overview of the thin film, (b) low magnification cross-section HAADF-STEM image of $NiTiO_3$ film, (c) High resolution HAADF-STEM image of the surface of single $NiTiO_3$ grain viewing along [110] zone axis. Noticed faceting of the grain along {014} and {015} planes, (d) high resolution HAADF-STEM image of the single grain along [100] zone axis. Magnified image together with overlapping simulated image and structural model are given in the insert. (e) high resolution HAADF-STEM image of the single grain along [210] zone axis. Magnified image together with overlapping simulated image and structural model are given in the insert. Image simulation was done based on IL structure.

Figure 7: TEM images of S2: $NiTiO_3$ thin film deposited on Si(100) substrate at 550°C and 1.5 Pa. (a) Low magnification HAADF-STEM image and simultaneously acquired EDX-STEM elemental maps for Ti K, Ni K, Si K. O K and overplayed color image. (b) high resolution [210] HAADF-STEM image of selected by black box in (a) area of $NiTiO_3$ film. The intergrowth secondary phase at $NiTiO_3$ grains boundaries marked by red arrows.

Figure 8: TEM images of S2: $NiTiO_3$ thin film deposited on Si(100) substrate at 550°C. (a) High resolution HAADF-STEM image of grain boundary region of $NiTiO_3$ film deposited at a pressure of 1.5 Pa and a substrate temperature of 550°C on Si substrate viewed along [210] zone axis. Red arrows depict the GBs (b) high resolution [210] HAADF-STEM image of $NiTiO_3$ grain and corresponding FT pattern. Simulated image based on LN structure is given in the insert in magnified image (left panel) (c) high resolution HAADF-MSTEM image of GB and corresponding FT pattern. The simulated image of GB structure based on $NiTiO_3$ CR is given in the insert. FT pattern is superposition of [210] $NiTiO_3$ LN (white rectangle) and [301] $NiTiO_3$ CR structure (red box).

Figure 9: SEM micrographs of thin films deposited simultaneously for 2 h at 1.5 Pa and 550°C :(a) as deposited and post-annealed under oxygen flow at (b) 600°C and (c) 800°C. (d)Diffraction patterns of these thin films

Figure 10: Raman spectra of thin films simultaneously deposited for 2 h at 1.5 Pa and 550°C and annealed under oxygen flow at 600°C and 800°C. A broken axis is used for the sake of clarity in order to suppress the very intense peak of Si substrate located at 520 cm^{-1}.

Figures

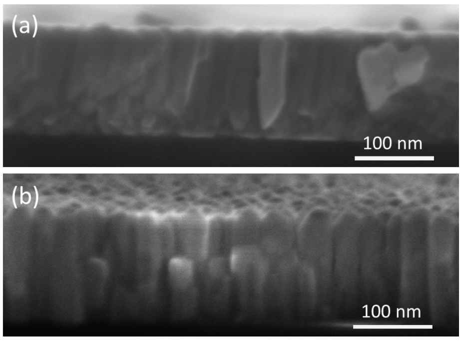

Figure 1: SEM cross section of NiTiO$_3$ *thin films deposited for 3 h at 550°C (a) and 650°C (b). The scale is indicated by the white bar. The thickness for each sample is estimated at 120 nm*

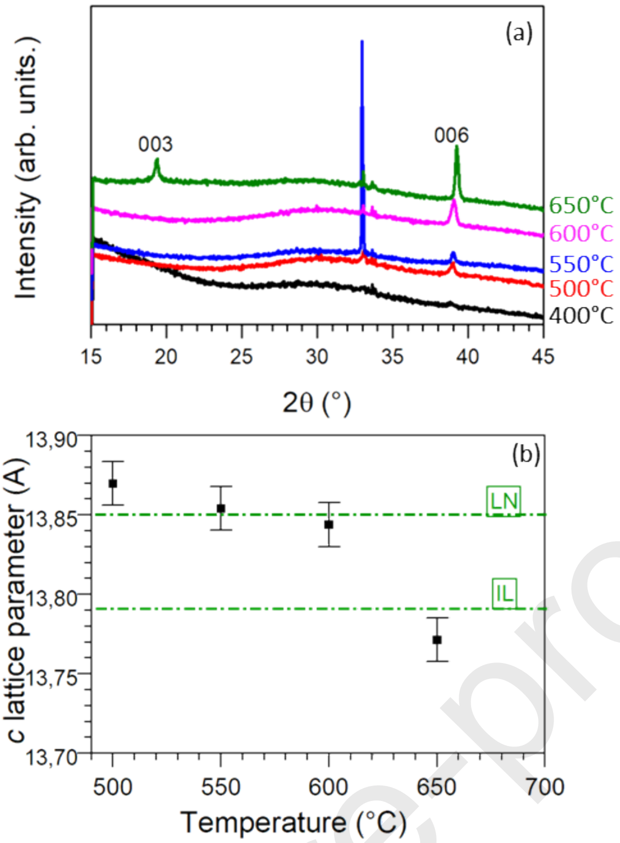

Figure 2: (a) XRD diffraction patterns of $NiTiO_3$ thin films, deposited at different temperatures (film thickness : 120 nm), (b) Out-of-plane lattice parameters c of the thin films of $NiTiO_3$ as a function of substrate temperature.

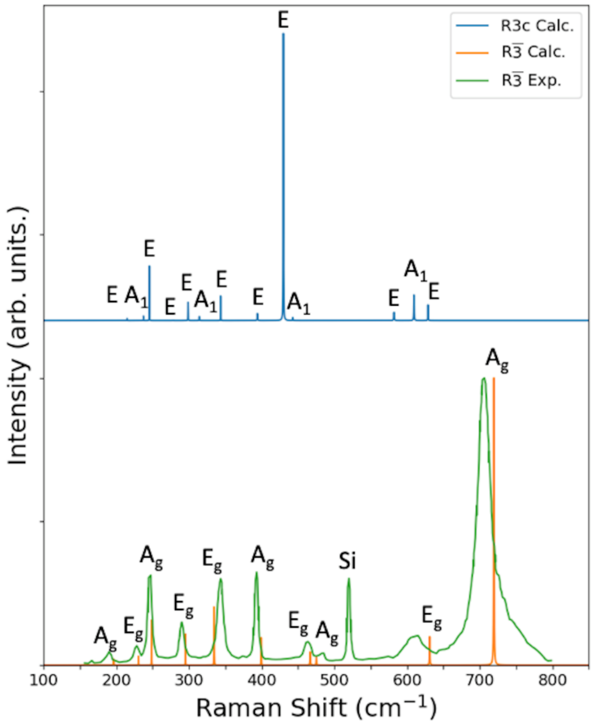

Figure 3: DFT simulations of the Raman spectra of both IL (R$\bar{3}$) and LN (R3c) phases of NiTiO$_3$. The experimental Raman spectrum of the IL phase is given for comparison. [56] The irreducible characters are provided. A scaling factor of 1.06 has been applied to the PBE+U values reducing the exp./theo. deviation from 24 to 1 cm^{-1} for IL phase. It allows to propose a prediction of the Raman shifts for LN phase. The calculation of the scaling factor was done using $s = \sum_i \left(w_i^{calc} w_i^{exp}\right) / \sum_i \left(w_i^{calc}\right)^2$*, with* w_i^{calc} *and* w_i^{exp} *the calculated and experimental frequencies, respectively, expressed in cm*$^{-1}$*. [57]*

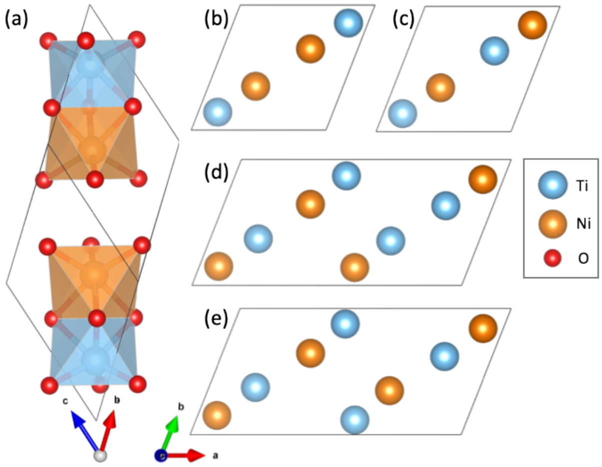

Figure 4: (a) Schematic representation of the primitive cell NiTiO$_3$ *in the IL phase along a axis. Views along c axis of (b) the IL phase, (c) the LN phase, and (d & e) the two CR models (oxygen atoms are not shown for simplicity).*

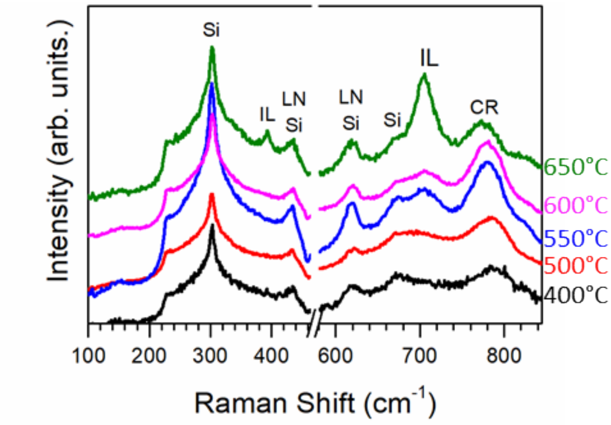

Figure 5: Raman spectra of thin films of $NiTiO_3$ *deposited at different substrate temperatures (from 400°C to 650°C). A broken axis is used for the sake of clarity in order to suppress the very intense peak of Si substrate located at 520* cm^{-1}.

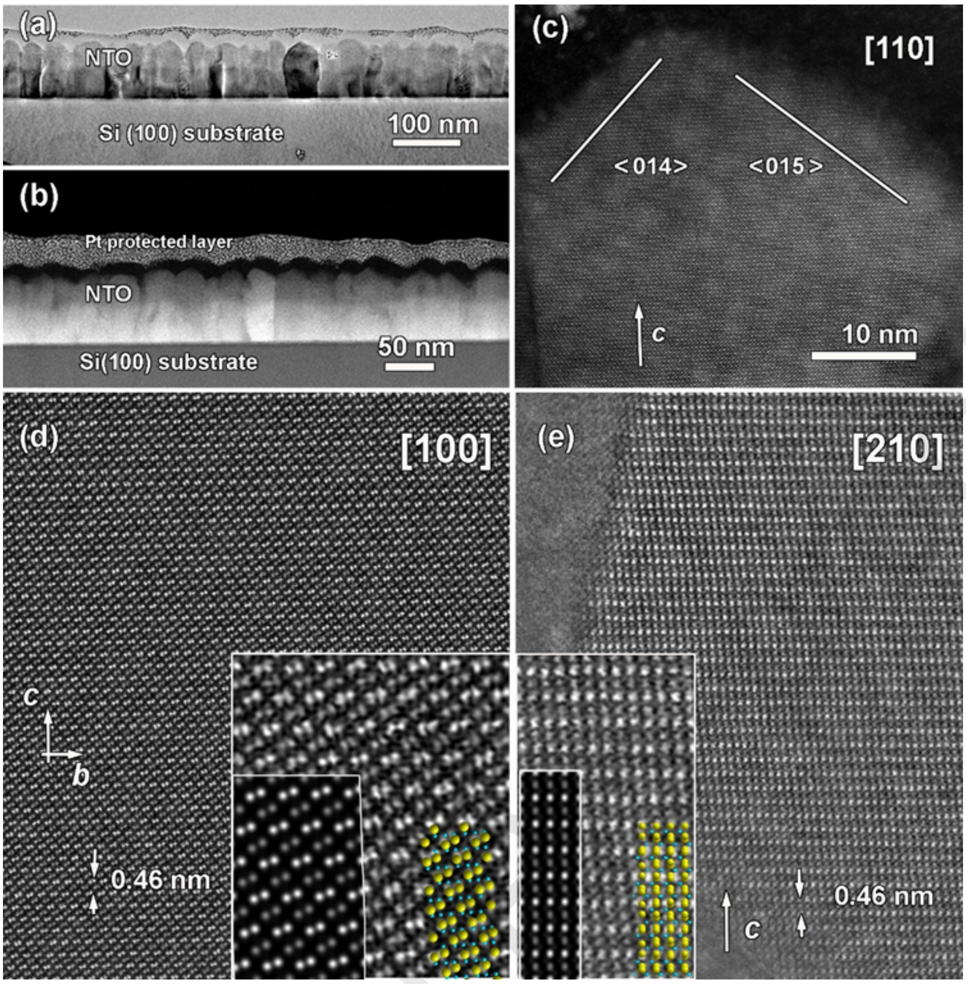

Figure 6: TEM images of S1: $NiTiO_3$ thin film deposited on Si(100) substrate at 650°C. (a) Cross-section bright field overview of the thin film, (b) low magnification cross-section HAADF-STEM image of $NiTiO_3$ film, (c) High resolution HAADF-STEM image of the surface of single $NiTiO_3$ grain viewing along [110] zone axis. Noticed faceting of the grain along {014} and {015} planes, (d) high resolution HAADF-STEM image of the single grain along [100] zone axis. Magnified image together with overlapping simulated image and structural model are given in the insert. (e) high resolution HAADF-STEM image of the single grain along [210] zone axis. Magnified image together with overlapping simulated image and structural model are given in the insert. Image simulation was done based on IL structure.

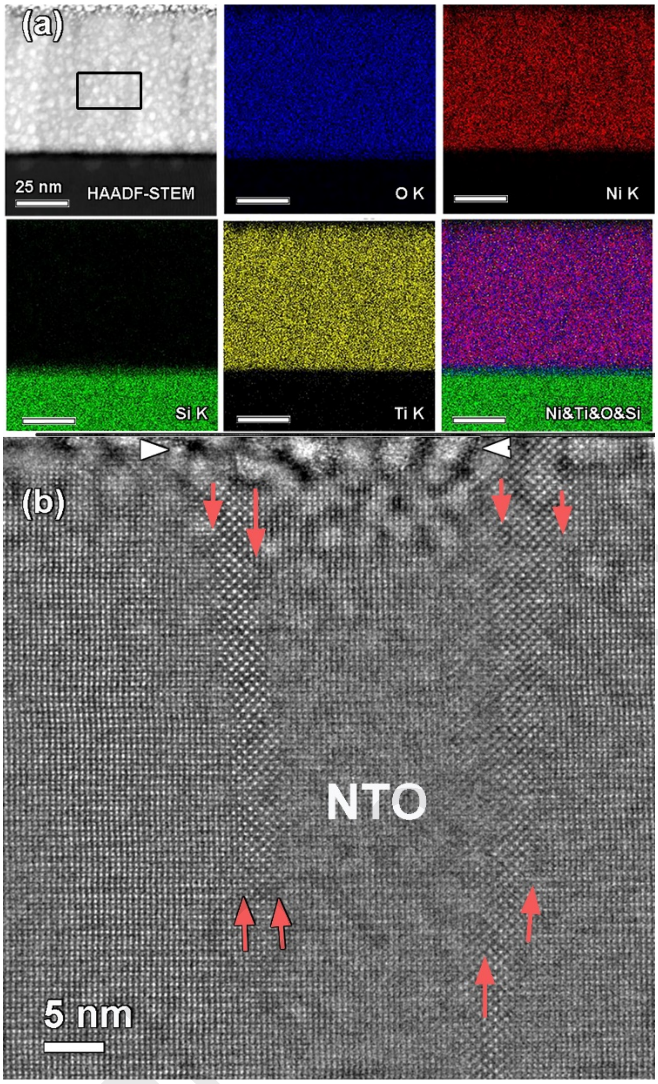

Figure 7: TEM images of S2: $NiTiO_3$ thin film deposited on Si(100) substrate at 550°C and 1.5 Pa. (a) Low magnification HAADF-STEM image and simultaneously acquired EDX-STEM elemental maps for Ti K, Ni K, Si K. O K and overplayed color image. (b) high resolution [210] HAADF-STEM image of selected by black box in (a) area of $NiTiO_3$ film. The intergrowth secondary phase at $NiTiO_3$ grains boundaries marked by red arrows.

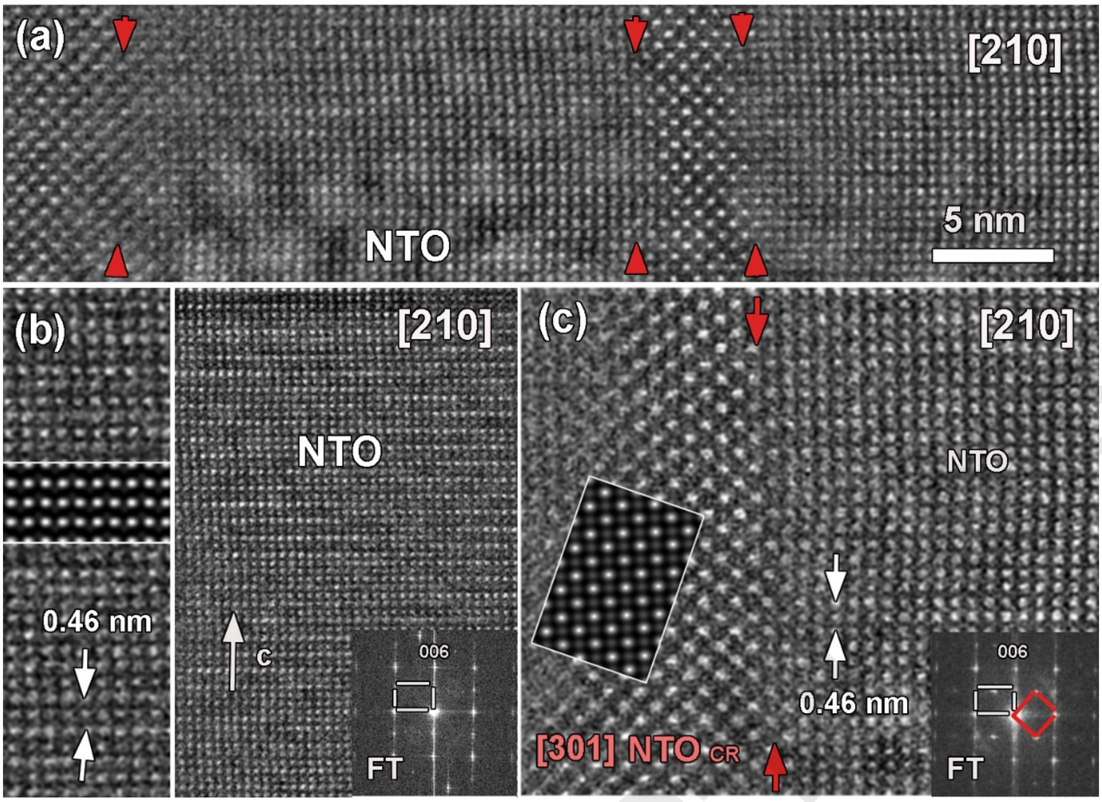

Figure 8: TEM images of S2: $NiTiO_3$ thin film deposited on Si(100) substrate at 550°C. (a) High resolution HAADF-STEM image of grain boundary region of $NiTiO_3$ film deposited at a pressure of 1.5 Pa and a substrate temperature of 550°C on Si substrate viewed along [210] zone axis. Red arrows depict the GBs (b) high resolution [210] HAADF-STEM image of $NiTiO_3$ grain and corresponding FT pattern. Simulated image based on LN structure is given in the insert in magnified image (left panel) (c) high resolution HAADF-MSTEM image of GB and corresponding FT pattern. The simulated image of GB structure based on $NiTiO_3$ CR is given in the insert. FT pattern is superposition of [210] $NiTiO_3$ LN (white rectangle) and [301] $NiTiO_3$ CR structure (red box).

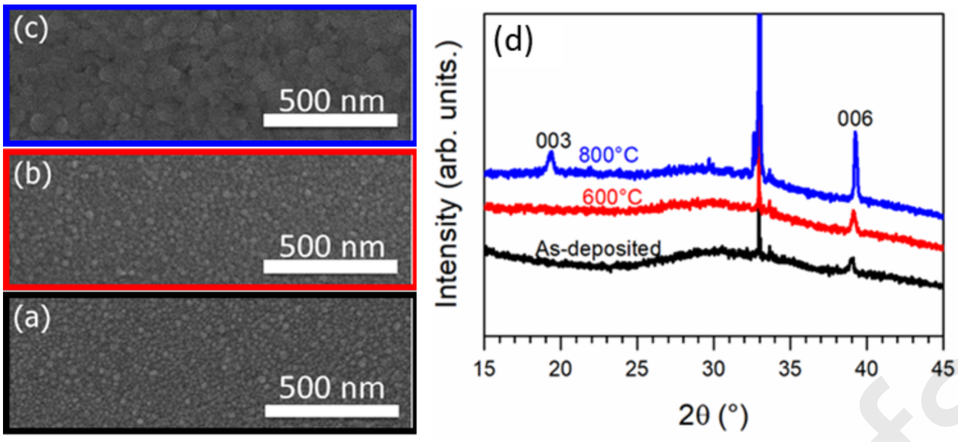

Figure 9: SEM micrographs of thin films deposited simultaneously for 2 h at 1.5 Pa and 550°C :(a) as deposited and post-annealed under oxygen flow at (b) 600°C and (c) 800°C. (d)Diffraction patterns of these thin films

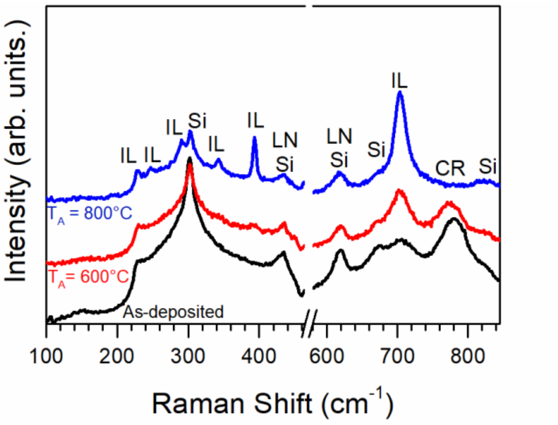

Figure 10: Raman spectra of thin films simultaneously deposited for 2 h at 1.5 Pa and 550°C and annealed under oxygen flow at 600°C and 800°C. A broken axis is used for the sake of clarity in order to suppress the very intense peak of Si substrate located at 520 cm^{-1}.

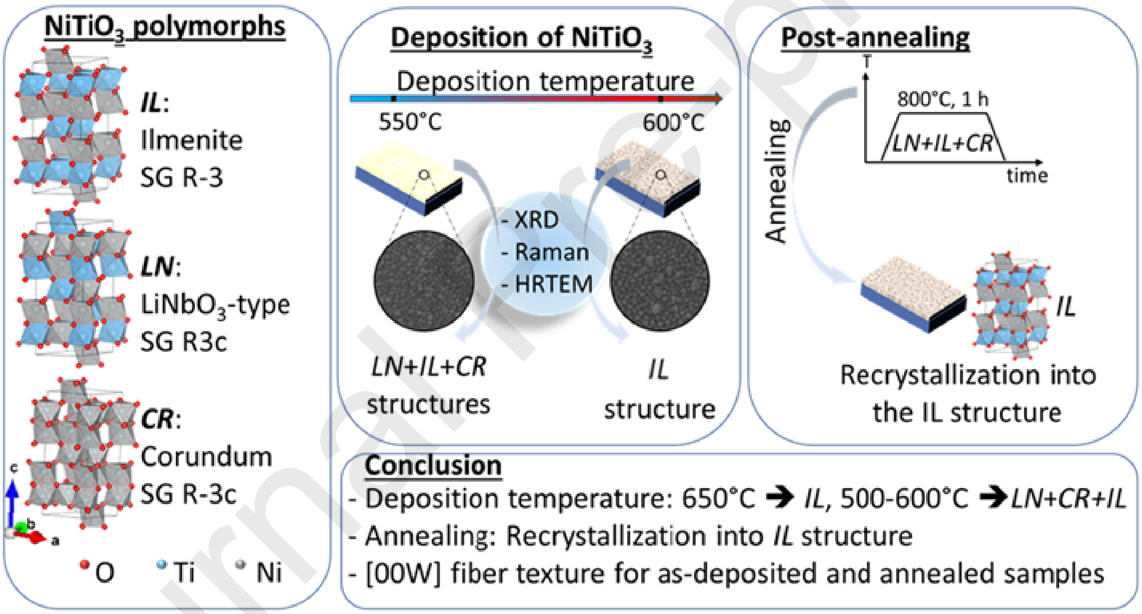

Conclusion

- Deposition temperature: 650°C → *IL*, 500-600°C → *LN+CR+IL*
- Annealing: Recrystallization into *IL* structure
- [00W] fiber texture for as-deposited and annealed samples

Highlights

- Deposition and growth conditions monitor the crystallographic structure of $NiTiO_3$ thin films structure via multitarget reactive RF magnetron sputtering
- First simulation of $NiTiO_3$ isomorphous to $LiNbO_3$-type Raman spectrum
- Multiscale characterization of $NiTiO_3$ enabled the differentiation between the three polymorphs of $NiTiO_3$ ($LiNbO_3$-type, Corundum, and IL)
- Post-annealing at 800°C transforms Corundum/$LiNbO_3$-type structures into IL structure